Rubber-Modified Glassy Amorphous Polymers Prepared via Chemically Induced Phase Separation. 2. Mode of Microscopic Deformation Studied by in-Situ Small-Angle X-ray Scattering during Tensile Deformation

B. J. P. Jansen, S. Rastogi,* H. E. H. Meijer, and P. J. Lemstra

Eindhoven Polymer Laboratories, The Dutch Polymer Institute, Eindhoven University of Technology, PO Box 513, 5600 MB, Eindhoven, The Netherlands

Received October 19, 2000

ABSTRACT: The mode of microscopic deformation in rubber-modified amorphous polymers has been investigated by small-angle X-ray scattering during tensile deformation. Synchrotron experiments were performed for blends consisting of poly(methyl methacrylate) (PMMA) with a finely dispersed rubbery epoxy phase. These blends were prepared via chemically induced phase separation, as shown in the first paper of this series. On macroscopic deformation these blends show that the toughness of brittle amorphous polymers can be significantly enhanced by the introduction of submicron size rubber particles. The objective of the present study is to establish the relationship between the morphology and the macroscopic mechanical properties of the blends. As observed for neat PMMA, crazing is found to occur for the macroscopically brittle PMMA/epoxy 90/10 blend. In contrast, the ductile blend with 20 wt % epoxy deforms via shear yielding which is preceded by cavitation. Shear yielding also occurs for blends having even higher epoxy contents, although it is not accompanied by the occurrence of dilatation processes. The changes in the scattering patterns during deformation are attributed to morphological changes like orientation. Cross-linking of the epoxy phase appears to have an important influence on the mode of microscopic deformation. A blend with 20 wt % un-cross-linked epoxy appears to deform via crazing instead of cavitation. The change in deformation mechanism is associated with the plasticization of crazes on a local level. The local strain is defined as the local deformation of the sample exposed to the incident beam as measured by recording the beam intensity in front of, and after, the sample during the drawing process. Thus, the local strain in the beam can accurately be measured and related to the corresponding scattering patterns. The local strain values obtained are in agreement with those from macroscopic tensile tests.

1. Introduction

Generally, the mechanical properties of brittle amorphous polymers are enhanced by the introduction of a dispersed rubbery phase. Toughness improvement in high-impact polystyrene (HIPS) is the result of multiple crazing on the microscopic level which is initiated by the presence of micron-sized rubber domains.[1] Recently, it has been shown that in polystyrene (PS) toughness enhancement can also be obtained by decreasing the absolute ligament thickness between rubber particles to a submicron level. In this case the improvement is the result of a transition in the mode of microscopic deformation from crazing to shear yielding.[2−4] These two examples indicate the importance of studying the mode of microscopic deformation and a necessity to establish the relation between the morphology and the mechanical properties of a blend, at both microscopic and macroscopic levels. In this study, the microscopic deformation of poly(methyl methacrylate) (PMMA) containing an extremely finely dispersed rubbery epoxy phase[5] is monitored in situ by performing small-angle X-ray (SAXS) experiments during tensile deformation. Time-resolved experiments were carried out using synchrotron radiation. SAXS as a tool to monitor deformation development at the microscopic level has been used earlier for both amorphous polymers[6−12] and semicrystalline polymers.[13−16] Detailed analysis of these SAXS data clearly results in more quantitative data, as compared to other techniques like dilatometry and microscopy.

For rubber-modified amorphous polymers, the occurrence of dilatation processes such as debonding, cavitation, and crazing can easily be distinguished from shear yielding. Crazing can be identified by SAXS as it results in typical crosslike scattering patterns consisting of two perpendicular streaks.[17,18] One is positioned along the tensile direction and the other perpendicular. The intense streak in the tensile direction, often indicated as “anomalous peak”, is the result of scattering caused by reflection from craze surface. The less intense streak, which develops parallel to the craze plane, is attributed to the scattering of the craze fibrils and can be used to calculate the amount of crazing and the craze fibril diameter.[6,7,19] In several synchrotron studies this fibril scattering is used to determine the contribution of crazing to the total amount of strain in rubber-modified thermoplastics.[6,7] Bubeck et al.[6] showed that, during impact deformation of HIPS and ABS (acrylonitrile−butadiene−styrene), only half of the total strain could be ascribed to crazing. Other dilatation processes and shear yielding accompany the remaining strain. He et al.[8,9] showed that the craze density decreases as the toughness increases in commercial rubber-toughened PMMA. The craze density was found to first increase and then decreases with increasing rubber particle concentration or cross-link density. Besides crazing, Lovell et al.[10] also observed other dilatation processes for rubber-modified PMMA which contained multilayered core−shell rubber particles. The scattering patterns found are ascribed to the occurrence of rubber particle cavitation and debonding. Earlier, Ijichi et al.

* To whom correspondence should be addressed.

10.1021/ma001810y CCC: $20.00
Published on Web 05/11/2001

Table 1. Overview of the Experimental Details for the Beamlines Used in This Study

	ESRF[24] (Grenoble, France)	CLRC[24] (Daresbury, UK)
beamline	ID2-BL4	Station 2.1
radiation wavelength [Å]	1	1.54
sample-to-detector distance [m]	8	9
beam size [mm^2]	0.5 × 0.5	3 × 1
collection time [s/frame]	30	20

reported rubber cavitation and debonding as the most important mode of microscopic deformation in rubber-modified blends of poly(phenylene ether) (PPE) and nylon-6.[11,12]

In the first part of this series of papers, the morphology and macroscopic mechanical properties of rubbery epoxy-modified PMMA have been discussed.[5] The blends were prepared via chemically induced phase separation which is used to produce extremely small rubber morphologies.[20] These morphology sizes can cause a toughness improvement as a result of the transition in mode of microscopic deformation from crazing to shear yielding. In uniaxial tension, the expected improvement has been observed for blends with a rubber fraction between 20 and 60 wt %. In contrast, during impact testing all blends with rubber fractions lower than 40 wt % fractured in a brittle fashion without any improvement in toughness. Remarkably, the impact toughness of the blend with 20 wt % rubber could easily be doubled by predeforming the sample in tensile at a limited deformation rate prior to impact testing.[5]

To explain the mechanical behavior observed, additional data concerning the relation between morphology, mode of microscopic deformation, and the resulting macroscopic properties are of most importance. Therefore, the microscopic deformation of these PMMA/epoxy blends is examined by using time-resolved SAXS experiments during slow speed tensile test. In a SAXS study, reported recently, the influence of an enhanced strain rate is examined to explain the contradiction in the measured tensile and impact toughness results.[21,22]

2. Experimental Section

2.1. Materials. The preparation, morphology, and properties of the PMMA/epoxy blends used in this study are discussed in the first part of this series.[5] All blends are prepared via chemically induced phase separation during the simultaneous polymerization of an initially homogeneous solution of methyl methacrylate (MMA) and an aliphatic epoxy resin. By a careful control over the system viscosity during phase separation, submicron morphologies were obtained.[5,20] Here, the following materials were used: PMMA/epoxy blends with 10, 20, 30, and 50 wt % epoxy resin, cast PMMA which was prepared via the same polymerization route, and a commercial PMMA grade (Atohaas, VO52) which was used for comparison.

2.2. Techniques. The mode of microscopic deformation of the blends was studied by performing time-resolved small-angle X-ray scattering (SAXS) measurement during tensile testing using the synchrotron radiation sources available at the ESRF (European Synchrotron Radiation Facilities, Grenoble, France) and the CLRC (Daresbury Laboratories, Warrington, United Kingdom). The experimental details of the two different beamlines used are summarized in Table 1. In both cases, scattering data were collected using a gas-filled multiwire two-dimensional (2D) detector. The test samples, as shown in Figure 1a, were stretched using a Rheometrics Minimat miniature tensile machine at a strain rate of 0.05 or 0.1 mm/min.

For experiments performed at the CLRC, the beam stop was positioned out of the center of the 2D detector, which allowed for the measurement of a larger range of scattering angles. Since the beam was rectangular in shape, the setup was equipped with a rectangular beam stop. To avoid experimental errors in measuring the scattered intensity, parallel and perpendicular to the tensile direction, the Minimat was tilted 45° from the vertical direction in the plane normal to the beam direction. This means that in the CLRC set up in Figure 1 the sample is rotated by an angle of 45° in the plane perpendicular to the paper. Accordingly, scattering patterns, as schematically shown in Figure 2, are also rotated by this angle of 45°. To convert the data into absolute intensities, the background scattering and the scattering of a reference sample were measured. As a reference sample, polyurethane (PUR) was used with known absorption coefficients. As PUR sample was a secondary standard, it was calibrated with a Lupolen standard.[23] Moreover, the total beam intensity in front of and behind the sample was recorded by ionization chambers during the complete drawing process (see Figure 1b).

3. Analysis

3.1. Analysis of Scattering Data. 3.1.1. A Comparison of Scattering Patterns for Deformation Mechanisms. The 2D X-ray scattering patterns presented in Figure 4 are measured using the ESRF facilities. The tensile direction is vertical. From the scattering patterns, three-dimensional azimuthal plots are constructed to visualize the development of orientation and dilatation during tensile deformation. To make a comparison, the raw data are first normalized by the simultaneously recorded beam intensity of the second ionization chamber,[24,25] in order to correct for sample thinning during deformation and the decreasing intensity of the X-ray source. Next, the data are divided by the detector response in order to correct for intrinsic errors in the intensity measurements of the detector used. Finally, the background scattering, which is mainly the result of air scattering, is subtracted.

The azimuthal dependence of the scattering pattern was assessed by subdividing the detector area into 90 sectors, each subtending 4° and integrating the scattered intensity over each sector (see Figure 2a). The distribution of the scattered intensity in the different directions relative to the tensile direction can be visualized by plotting the integrated intensity against the azimuthal angle (see Figure 2b). Intensities at 90° and 270° correspond to the tensile direction, whereas those at 180° are related to the perpendicular direction. A three-dimensional plot can be constructed by using the deformation time as third axis, as for example in Figure 5a. It is to be noted that from here no quantitative data analysis can be performed. These plots have been made only to follow changes occurring along equatorial and meridonial directions with the development of different deformation mechanisms like craze formation, cavitation, or shear yielding processes.

3.1.2. Determination of the Fibril Diameter within Crazes. The same materials were measured again at the CLRC to confirm the earlier observations at the ESRF and to collect a complete set of data that can be analyzed in terms of absolute intensities. Similar to ESRF data, CLRC data were first normalized, divided by detector response and corrected for background scattering. The resulting scattering data are converted to absolute values by multiplying the data by a conversion factor which is derived from the measurements of the PUR reference sample, calibrated with the Lupolen sample, with known absolute intensity;[25] thus, it was

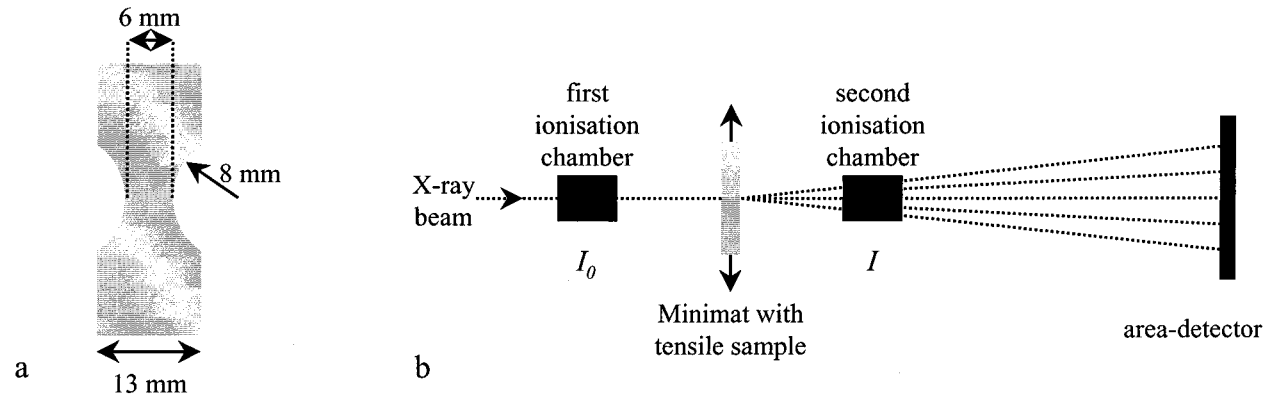

Figure 1. Schematic representation of (a) test bars used in the simultaneous SAXS tensile experiments and (b) the experimental setup at the CLRC/ESRF. In CLRC the setup stretching device was tilted by 45° in the plane normal to the beam direction.

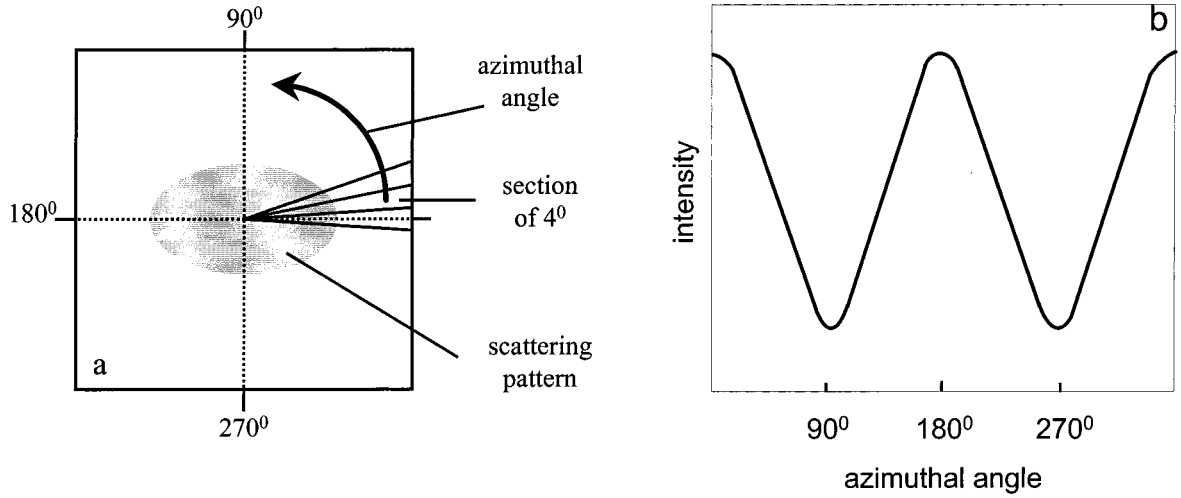

Figure 2. Schematic representation of data analyses as performed for the ESRF measurements. (a) Division of the 2D scattering patterns in 4° sections and (b) the resulting azimuthal plot which describes the relation between the intensity and the azimuthal angle. Overall integrated intensity along the azimuth angle, with drawing of the sample is shown in figures like Figures 5a, 7a, 9a, 10, and 11a.

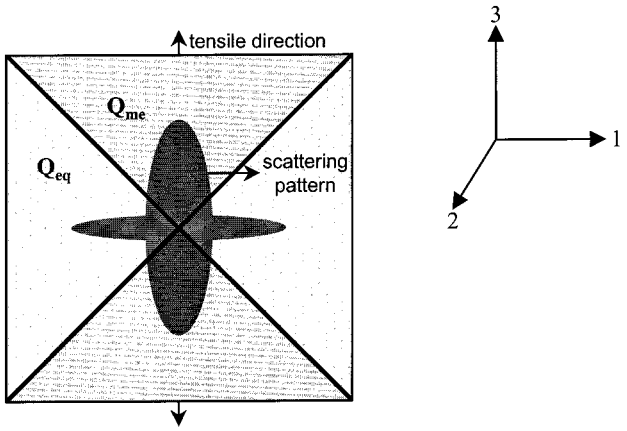

Figure 3. Schematic representation of data analyses as performed for the CLRC measurements. The intensity was integrated from 315° to 45° for determining the intensity development perpendicular to the draw direction and 45° to 135° for evaluating intensity development along the tensile direction, as shown in Figures 5b, 7b, 6a, 6c, and 9b. The absolute invariant (Q_{eq}) perpendicular to the tensile direction is calculated separately from the SAXS patterns.

possible to make a proper comparison between differentsamples. However, it was not convincingly possible to convert the scattered intensity into the number of photons; therefore, true values for the absolute intensity are not mentioned in the figures.

To monitor craze formation, cavitation, and/or orientation, the intensity distribution, parallel and perpendicular to the tensile direction, is followed by integrating the intensity. On the other hand, fibril diameter is determined by calculating an invariant perpendicular to the draw direction.

Before we calculate an invariant, it is important to discuss the optics for the beam collimation, the detector used for data collection, and the scattering laws which can be used for the present setup. To do so, it is important to highlight the developments which have taken place in past, in terms of data collection and respective data analysis.

In the pioneering work, Kramer and co-workers[6,7] used synchrotron radiation available at CHESS, Cornell. They used a pinhole collimator to get a 300 μm primary beam. The data acquisition was done on a linear 1024-element X-ray sensitive Reticon diode array. The detector was mounted perpendicular to the stretching direction of the sample; thus, the scattered intensity from the craze fibrils could be recorded only, and since the intensity parallel to the draw direction could not be recorded, the scattered intensity arising from reflection of the craze surface was not taken into consideration. Kramer and co-workers[6,7] could make use of the mathematical expressions which are usually applicable for a primary beam obtained from an infinite slit geometry since their experimental setup had a point

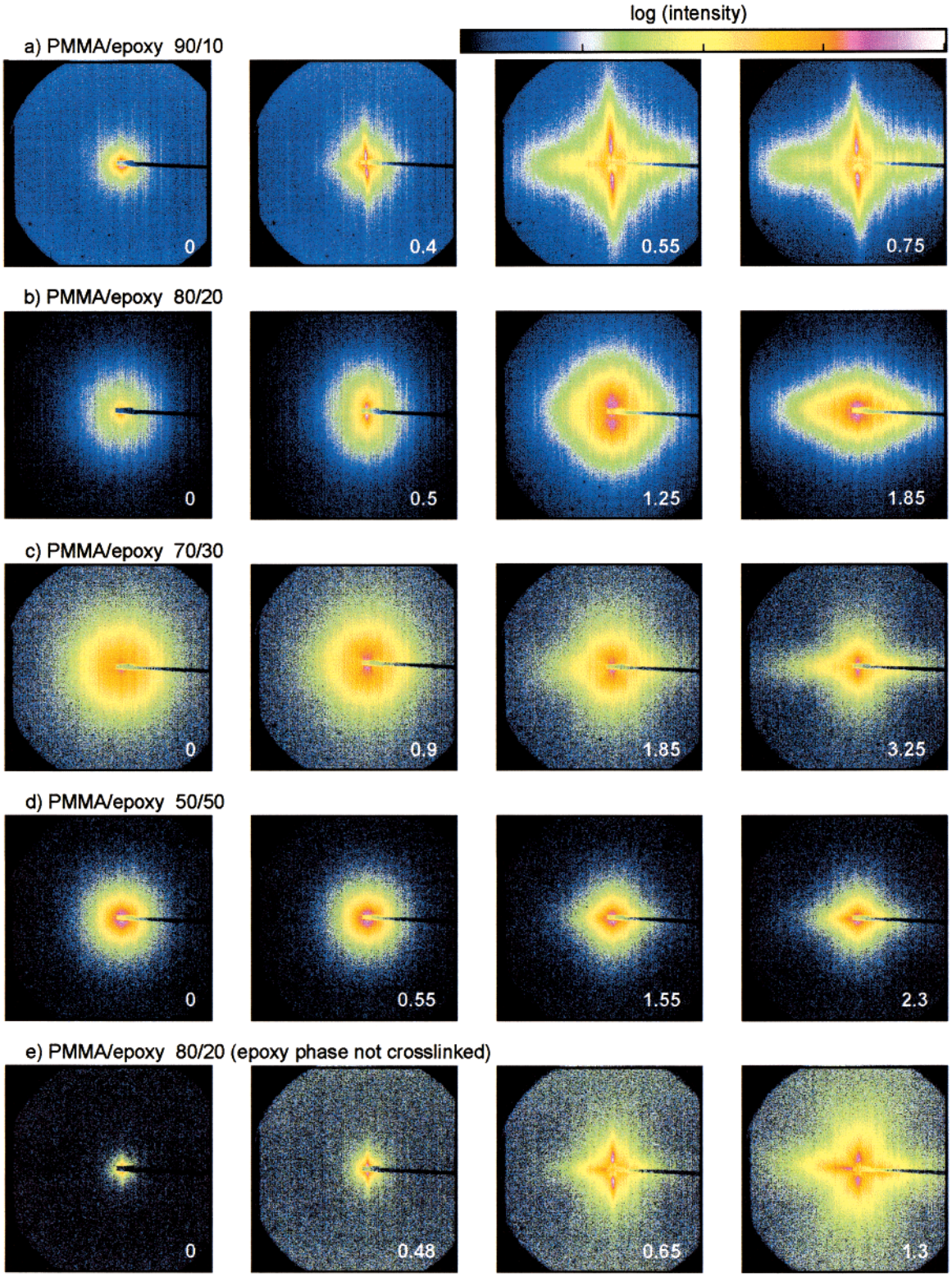

Figure 4. Deformation SAXS patterns of PMMA/epoxy blends measured at different clamp displacements, x [mm], indicated in the right bottom corner. Experiments performed at the ESRF, ID2-BL4. Tensile direction is vertical.

collimated beam, and they measured the scattered intensity on a slit-collimated detector, placed perpendicular to the draw direction.

As linear detectors have been replaced by two-dimensional detectors, it has been possible to measure the scattered intensity simultaneously along the perpendicular, as well as along the draw direction. A question which needs to be resolved is how to deconvolute the scattered intensity perpendicular and parallel to the draw direction. A rigorous solution to this has been proposed by Stribeck[26,27] which may be summarized as follows. For the case of the strained samples, as happens to be the case during drawing experiments, one observes scattering patterns with cylindrical (fiber) symmetry. Because spherical symmetry is more than fiber symmetry, all the mathematics can be performed in cylindrical coordinates. So, it is reasonable to write intensity as a function of cylindrical

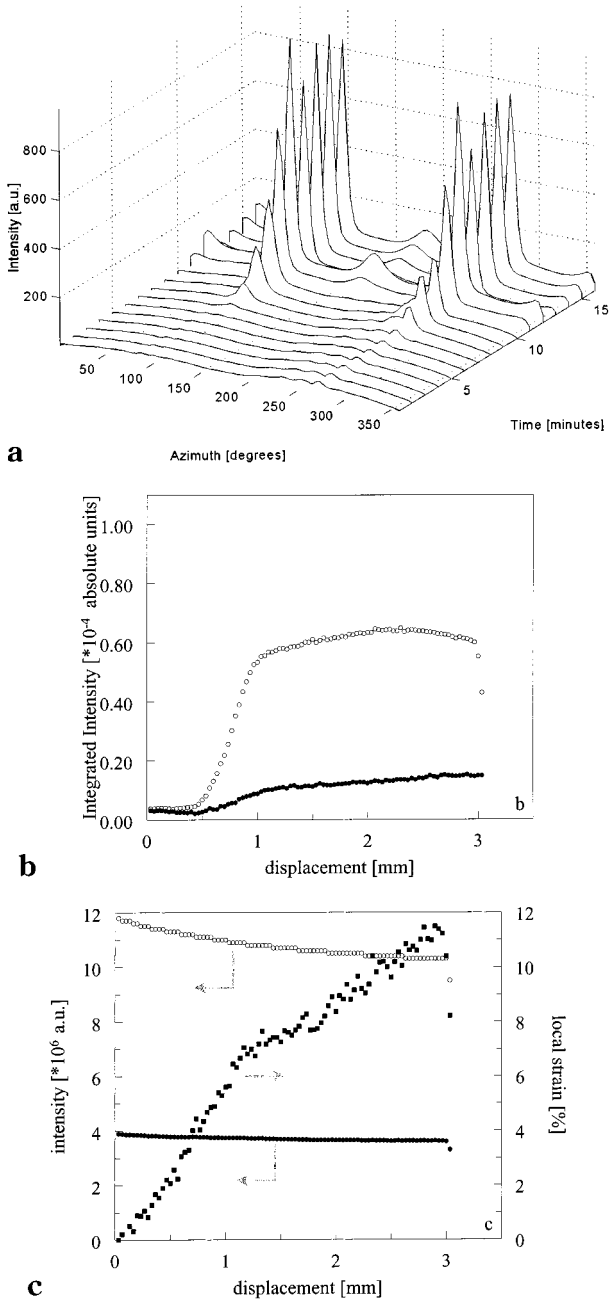

Figure 5. SAXS data for the in-situ deformation of PMMA/epoxy 90/10, stretching speed of the sample was 0.1 mm/min: (a) azimuthal plot (ESRF); (b) absolute intensity integrated perpendicular (●) and parallel (○) to the tensile direction vs the clamp displacement (CLRC). The integration has been performed within the regions discussed in Figure 3. (c) Local strain (■), intensity of the first (○) and second (●) ionization chamber vs the clamp displacement (CLRC).

coordinates, i.e.

$$I(\vec{s}) = I(s_{12},s_3) = I(s_\perp,s_{||}) \tag{1a}$$

In any nomenclature, the invariant $Q = \int I(\vec{s})\ \mathrm{d}^3s$ is valid. So by definition there is no orientation dependence of Q. For an oriented sample like ours, discrimination between two components (parallel and perpendicular to the draw direction) contributing to scattering which show up in the two different regions of reciprocal space can be made. Thus, a border can be defined between scattered intensity along and perpendicular to the draw direction (as schematically shown in Figure 3), and it is feasible to integrate each of the subspaces separately. Therefore, it should now be possible to discuss two different kinds of Q values: one arising from the "equatorial streak component" and the other originating from the residual scattering. The equatorial streak component is of interest to us for quantitative analysis, i.e., determination of craze fibrils, a point to which we will arrive later.

After subdivision of reciprocal space, the second step is to extract quantitative information from the scattered intensity. This can be done for both the subspaces for Q_{eq} (invariant calculated along the equator, perpendicular to the draw direction) and Q_{me} (invariant calculated along the meridian, parallel to the draw direction) by dividing the patterns in two sections of 90° (see Figure 3). For the calculation of the intensity within subsections, each of them was further divided in sectors, each of 4° as shown in Figure 2. Integration along the individual sectors was performed, which may be presented mathematically as follows:

$$I(s_3) = 2\pi \int_{s_{12}=-s_3}^{s_{12}=s_3} s_{12} I(s_{12},s_3)\ \mathrm{d}s_{12} \tag{1b}$$

$$I(s_{12}) = \pi s_{12} \int_{s_3=-s_{12}}^{s_3=s_{12}} I(s_{12},s_3)\ \mathrm{d}s_3 \tag{1c}$$

Limits of the integrals are from −45° to 45° as shown in Figure 3 for two different reciprocal subspaces. The two components of Q are computed by integrals of identical form, along the reciprocal spaces as defined along the equator and the meridian, in Figure 3.

$$Q_{eq} = 2\int_0^\infty I(s_{12})\ \mathrm{d}s_{12} \tag{1d}$$

$$Q_{me} = 2\int_0^\infty I(s_3)\ \mathrm{d}s_3 \tag{1e}$$

Substitution of eqs 1b and 1c in eqs 1d and 1e gives rise to double-integral equations for the invariants along the equator and meridian defined as Q_{eq} and Q_{me}.[28]

Since the invariant from experimental data is collected within a finite interval, extrapolation of the intensity from s_{max} (maximum measured angle) to infinity and s_{min} (minimum measured angle) to zero angle is required. Extrapolation from s_{min} to zero angle was performed by extrapolating a plot of $s^*I(s)$ vs s to zero. Whereas, from s_{max} to infinity, an extrapolation was performed using Porods' law (i.e., by extrapolating a plot of $s^3I(s)$ vs s^3), the law discussed below. In the case of systems, which deform via crazing, the craze fibril diameter, D, was calculated using[29]

$$D = \frac{1}{\pi^3(1-\nu)} \frac{Q_{eq}}{k} \tag{2}$$

where ν is the volume fraction fibrils in the craze and Q_{eq} is the invariant of the scattering caused by the craze fibrils.[17] The scattered pattern used for this purpose is the one recorded after complete stretching of the sample, where crazes and the craze fibrils were oriented in the draw direction. In the perfectly aligned fibril case, the intensity arising from fibrils is a disk in reciprocal space; thus, eq 1e which has notations for a disk in the reciprocal space can be used. The Porod constant, k, was obtained by making a plot of Is^3 vs s^3, a justification for the use of this formulas for the system and the experimental setup like ours is given below. Opposed to Q_{eq},

no quantitative analysis could be made from Q_{me}, since the intensity along the meridian arises from reflected intensity originating from the surface of crazes[6,7,18] and thus has no physical significance.

Since we have integrated the intensity along a reciprocal subspace within the quadrant region, as shown in Figure 3, the data though recorded on a quadrant region of the detector have been converted in the equivalence of a linear detector. Since data collection is, using a point collimation beam, effectively the same as for a linear detector, giving the arguments here that are similar to those of Kramer and co-workers[6,7] as well as He, Donald, and Butler,[8,9] it is possible to use the scattering laws applicable to an infinite slit geometry. If the scattering objects are isotropically distributed, as in the case of a sphere, the intensity will vary with s^{-4}, whereas if objects are anisometric in nature (like having a cylindrical geometry), the intensity variation[30] would be s^{-3} as opposed to s^{-4}.[31]

In crazes like those present in our system, fibrils are oriented regularly along the draw direction. The craze fibrils present within the crazes have a cylindrical geometry. Since we were interested in determining the diameter of craze fibrils, we had to make use of Porod's law, which holds for a cylindrical geometry. Using similar arguments, by drawing a plot of Is^3 vs s^3, the Porod constant, k, was also obtained by Kramer and co-workers[6,7,18] as well as Donald and co-workers.[8,9,13−15]

3.2. Analysis of Strain Data. Considering the adjusted sample geometry and the limited size of the beam, care should be taken in the interpretation of the scattering data in relation to the macroscopic strain or displacement of the stretching device. Therefore, we related the 2D scattering patterns to the actual local strain, as viewed by the beam, calculated by using the intensities measured by the ionization chambers (see I_0 and I in Figure 1b). This allows for a direct comparison of the local strain data and the X-ray scattering patterns measured. One needs to take into consideration that the transmitted primary beam remains unaffected by the morphological changes that the primary beam encounters, although the scattered intensity will change. This consideration is valid within the experimental limitations of the ionization chambers, as the primary beam is much stronger than the scattered intensity.

The strain, ϵ, of a volume element is defined as

$$\epsilon = \left(\frac{l_t}{l_0} - 1\right) \times 100\% \tag{3}$$

where l_0 and l_t are the lengths of the volume element in the tensile direction at time $t = 0$ (before deformation) and at time t (during deformation), respectively. If introduced voids are excluded, the volume of the deforming material is constant,

$$w_0 d_0 l_0 = w_t d_t l_t \tag{4}$$

where w and d are the width and thickness of the volume element. By assuming that the contraction in both directions perpendicular to the tensile direction is the same, the local strain equals

$$\epsilon_{local} = \left[\left(\frac{d_0}{d_t}\right)^2 - 1\right] \times 100\% \tag{5}$$

In contrast to the length, l, which is drawn out of the beam spot, the thickness, d, can be measured during the complete deformation process. Hence, the local strain can exclusively be calculated from this parameter which can be described by the changes in the absorbed radiation. The absorption equals

$$I = I_0 e^{-ad_t} \tag{6}$$

where a is the adsorption coefficient of the sample which can be determined by using the boundary condition for the thickness prior to deformation, $d_t = d_0$:

$$\frac{I_0}{I} = \frac{(I_0)_{t=0}}{(I)_{t=0}} \tag{7}$$

It can be derived that

$$\frac{d_0}{d_t} = \frac{\ln(I_0)_{t=0} - \ln(I)}{\ln(I_0) - \ln(I)} \tag{8}$$

Thus, on substituting eq 8 in eq 5, the local strain can directly be calculated from the changes in sample thickness during deformation. Note that the occurrence of dilatation processes, like crazing and void formation, is of no relevance since the sample thickness is measured by using the beam intensities, i.e., by measuring the absorption directly. Therefore, these calculations can also be used for systems that deform via crazing or rubber cavitation and/or debonding. Hence, the *effective* local thickness, which is obtained using this method, will not necessarily be equal to optical macroscopic sample thickness.

The approach proposed here for determination of the local strain can be adopted in general for all materials—ranging from polymers to metals or composites. However, in metallic compounds, multiple scattering can become rather significant, and the approach will certainly have its limitations.

4. Results and Discussion

As discussed in an earlier paper, the PMMA/epoxy blends used demonstrate a remarkable synergistic toughness under both tensile and impact conditions.[5] For the blends, which contain only 10 wt % of rubbery epoxy or less, no separate rubber morphology was found, and all samples suffered from brittle failure at limited deformation. The PMMA/epoxy 80/20 blend behaves more ductile upon tensile testing and shows stress whitening during deformation. In contrast, the blends with 70−50 wt % PMMA, which possess the highest tensile toughness, deform via homogeneous contraction over the whole sample without any stress whitening. As the rubber content is increased even further, the tensile toughness decreases again as a result of the brittle behavior of the pure epoxy rubber.

Depending on the mode of microscopic deformation, the blends investigated can be divided into three categories, i.e., crazing, cavitation, and shear yielding, which will be discussed separately below. Finally, the influence of cross-linking of the epoxy phase on the microscopic deformation is evaluated.

4.1. Microscopic Deformation of the Brittle Systems. Figure 4a shows the development of the 2D scattering pattern during tensile deformation of the brittle PMMA/epoxy 90/10 blend. Since this blend is homogeneous, hardly any scattering is observed prior to deformation; displacement $x = 0$ mm. During defor-

mation, intense scattering streaks are developed in the tensile direction; see $x = 0.4$ mm in Figure 4a. Upon further drawing, an additional but less intense scattering streak develops perpendicular to the tensile direction; see $x = 0.55$ and $x = 0.75$ mm. As discussed in the Introduction, the crosslike pattern obtained can be ascribed to the scattering of crazes.[17,18] The intensity of the streak in the tensile direction is clearly stronger compared to the scattering resulting from the craze fibrils which is also obvious from the azimuthal plot in Figure 5a. The peaks at 90° and 270°, which correspond to the tensile direction, are much more intense compared to the one at 180°, which results from the craze fibril scattering. Of course, the same trend is observed for the integrated intensities, parallel and perpendicular to the tensile direction, which are plotted as a function of the clamp displacement in Figure 5b.

Figure 5c shows the relation between the clamp displacement and actual local strain in the beam calculated from the intensities measured by the ionization chambers using eqs 5 and 8. Initially between 0 and 0.5 mm displacement, the local strain increases with the clamp displacement (Figure 5c) without the occurrence of any scattering (Figure 5b). The absence of scattering in this region suggests that the local strain measured is the result of sample thinning. The development of scattering beyond a displacement of 0.5 mm, which corresponds to a local strain of ~2.5%, is associated with the onset of craze formation. The local strain measured during the complete experiment can be divided roughly in two regions with different slopes, for example above and below 1.4 mm displacement in Figure 5c. This indicates a difference in local strain rate, which appears to be higher for the initial stage. During the deformation at higher strain rate, a strong increase in the integrated intensities is observed between a displacement of 0.5−1.2 mm. This can be explained by the nucleation and growth of crazes.

In contrast, in the second region, i.e., between 1.2 and 3.0 mm displacement, which corresponds to a lower local strain rate, hardly any changes in the integrated intensities are observed. The constant integrated intensities suggest that the scattering intensity from the crazing process does not vary within the scattering region measured experimentally. This indicates that no new crazes are formed. Nevertheless, the local strain still increases which can simply be explained by sample thinning and/or by the growth of already formed crazes. However, the scattering from the changes in these crazes cannot be measured within the experimental scattering region.

The difference in local strain rate between the two regions discussed can be explained by the localization of deformation in the sample. Apparently, after the crazes are formed within the first region, most of the deformation occurs mainly outside the beam spot that results in a reduced local strain rate for the second region.

For comparison, the integrated intensity and strain data for neat PMMA, both cast and extrusion grade, are depicted in Figure 6 with the same values for the displacement axis. The differences in integrated intensities and local strain between the two are limited. Although, the displacement might suggest a higher strain for cast PMMA, the local strain at break is almost the same (compare Figure 6b and 6d). The absolute values of the integrated intensity resulting from the craze fibril scattering are even lower compared to the PMMA/epoxy 90/10 system, which indicates a lower craze fibril density (compare Figures 5b, 6a, and 6c). Although the 90/10 blend is homogeneous and does not possess any craze initiating rubber particles, the tendency for crazing appears to be stronger in comparison to neat PMMA. Moreover, the crazes formed are relatively stable resulting in a higher clamp displacement at fracture. The local strain at break of neat PMMA corresponds with the local strain at the end of region one for the 90/10 blend, which is related to the nucleation and growth of crazes. However, in the case of neat PMMA, fracture occurs immediately after the nucleation and growth of the crazes while the stability of the crazes in the 90/10 blend results in a larger deformation volume and, subsequently, in an improvement of the local strain at break from approximately 7 to 12%.

4.2. Ductile Blends Deforming via Cavitation. Of all PMMA/epoxy blends, the ductile 80/20 blend is the only one which shows stress whitening during tensile deformation. The mode of microscopic deformation is clearly different from the 90/10 blend as can immediately be concluded from the development of the scattering patterns in Figure 4b. Initially, again hardly any morphological scattering is observed. At $x = 0.5$ mm some additional scattering is found in the tensile direction, accompanied by some orientation as can be concluded from the slightly elliptical scattering pattern. At $x = 1.25$, a more symmetric pattern can be observed as the scattering perpendicular to the tensile direction is enhanced. This is, finally, followed by an extensive orientation which results in the strong elliptical scattering pattern as found for $x = 1.85$.

The azimuthal plot for this blend is also very different from those of the brittle crazing systems discussed above (see Figure 7a). As observed for the formation of crazes, also in this case some enhanced scattering in the tensile direction is observed. For the 80/20 blend, however, this is followed by an overall increase in intensity, indicating the development of electron density fluctuations. With increasing draw ratio, the following decrease in the intensity of the peaks at 90° and 270°, and the subsequent increase at 180°, indicates the redistribution of the scattered intensity from the parallel to the perpendicular tensile direction as expected from the development of the elliptical scattering pattern. The most plausible explanation in terms of the development of microscopic deformation phenomena for the observed scattering patterns is schematically represented in Figure 8. First some cracklike voids, or maybe even a limited amount of crazes, are formed, causing the additional scattering in tensile direction. Next, the formation of numerous voids causes the increase in overall intensity. As the voids will relieve the triaxial stress state in the blend, shear yielding is enhanced[33,34] which allows further deformation and, consequently, orientation of the voids in the tensile direction. The changes in the principal axis of the orienting voids results in the development of the ellipsoidal scattering pattern and thus in a redistribution of the intensity.

Figure 7b shows the development and distribution of the absolute integrated intensity values in the directions relative to the tensile direction. The relative difference between the integrated intensities is less compared to the brittle systems which deform via crazing. Both integrated intensities clearly show a maximum which is the result of the decreasing amount of scattering units

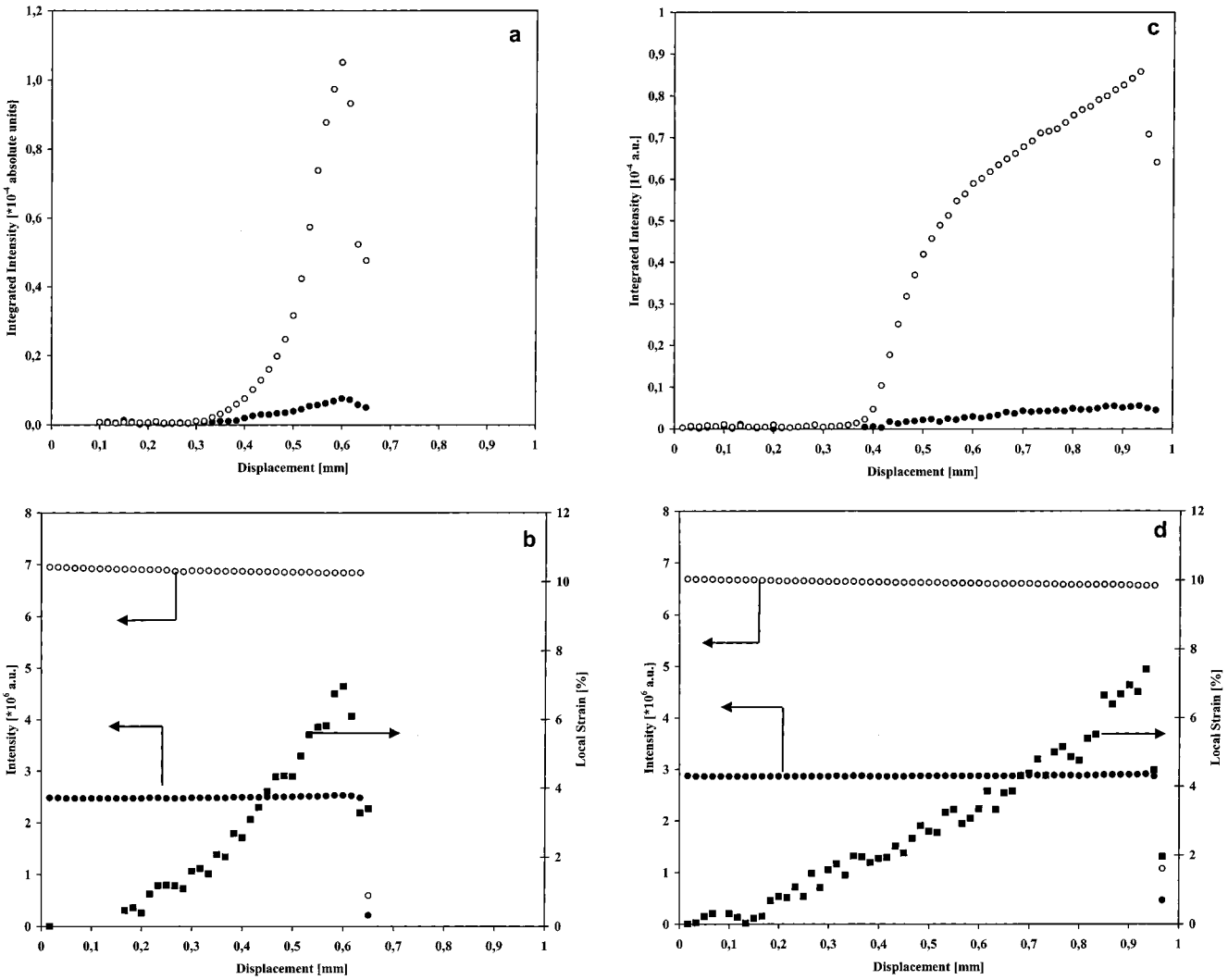

Figure 6. (a) Absolute intensity integrated perpendicular (●) and parallel (○) to the tensile direction vs the clamp displacement for cast-PMMA (CLRC). (b) Local strain (■), intensity of the first (○) and second (●) ionization chamber vs the clamp displacement for cast PMMA (CLRC). Comparable graphs for the integrated intensity and local strain data of a PMMA extrusion grade are respectively shown in (c) and (d).

in the beam as the samples thickness decreases upon further drawing. The decreasing absorption caused by this thinning process does not contribute to the observed maxima since the scattering data have been normalized to the second ionization chamber. Still, the ongoing orientation of the voids upon drawing is evident from the crossing over of the integrated intensities.

The absolute integrated intensity values are several times larger in comparison to the 90/10 blend, which indicates the occurrence of much more dilatation processes during deformation. However, this is accompanied by a much larger local strain of 150% (see Figure 7c), which is even higher than the strain calculated from the fracture surfaces in the macroscopic tests (for comparison, see Figure 10b in ref 5). This difference is a result of the fact that the local strain is calculated via the intrinsic thickness measured by the ionization chambers which excludes the voids formed during deformation. As can be observed in Figure 7b,c, the deformation in the beam is only initiated after a clamp displacement of 1 mm. The local strain rate beyond a displacement of 1 mm is relatively constant and only slowly decreases toward the end of the experiment. The strength of the proposed local strain calculation method is demonstrated by the last data points, indicated by the arrow, which show a sudden drop in the local strain while the values of the integrated intensities are retained. The decrease can be explained by the initiation of a macroscopic crack outside the beam spot which partially relieves the elastic strain and, subsequently, causes thickening of the sample inside the beam. Release of the elastic strain is also the reason for the minor changes observed in the integrated intensity values.

4.3. Ductile Blends Deforming without Cavitation. The PMMA/epoxy blends containing 30−60 wt % epoxy behave ductile during tensile deformation without any stress whitening. In contrast to the blends discussed above, the scattering patterns of the PMMA/epoxy 70/30 do not show any dramatic changes as a result of the occurrence of dilatation processes (see Figure 4c). The changes observed in the scattering patterns are caused by the orientation of the rubber morphology. As for the previously discussed blends, first (x = 0.9 mm) some additional scattering is concentrated in the tensile direction which is followed by the intensity development in the perpendicular direction (x = 1.85 mm). Upon further drawing the intensity concentrates parallel and perpendicular to the tensile direction. As confirmed by the azimuthal plot (Figure 9a) and the integrated

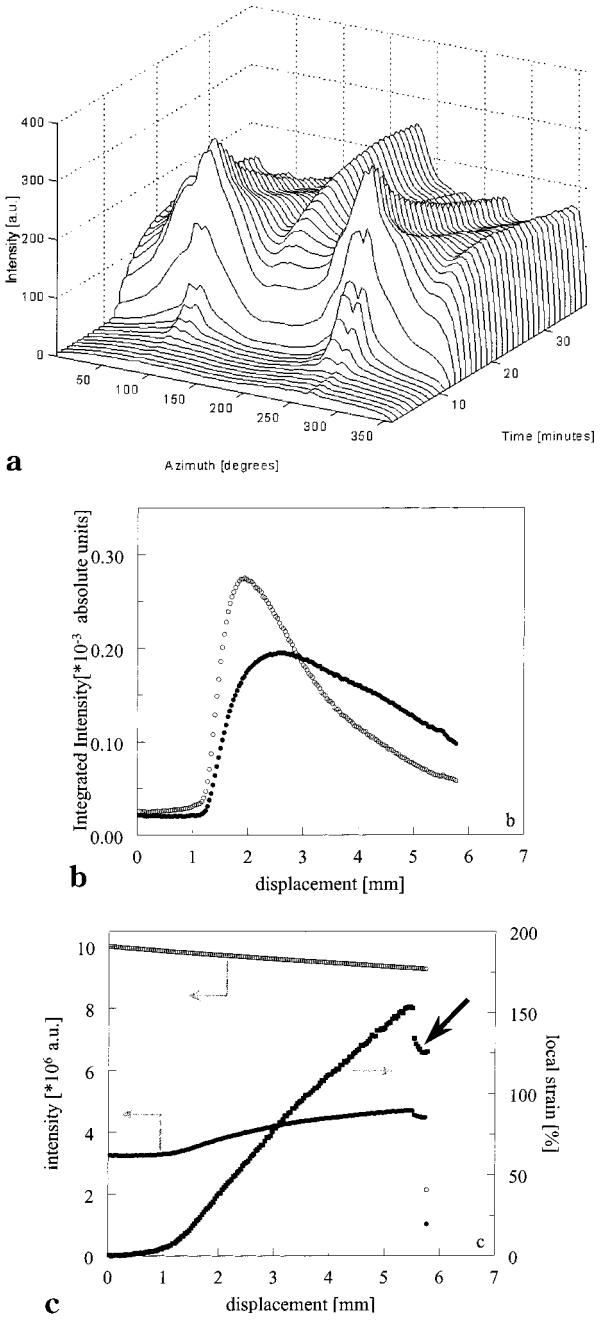

Figure 7. SAXS data for the in-situ deformation of PMMA/epoxy 80/20, stretching speed of the sample was 0.1 mm/min: (a) azimuthal plot (ESRF), (b) absolute intensity integrated perpendicular (●) and parallel (○) to the tensile direction vs the clamp displacement (CLRC), (c) local strain (■), intensity of the first (○) and second (●) ionization chamber vs clamp displacement (CLRC).

intensities (Figure 9b), the overall intensity decreases toward the end of the drawing process. This can again be explained by sample thinning which results in a decreasing amount of scattering units in the beam.

Nevertheless, initially at 1 mm displacement, a slight maximum is observed in both the intensity (Figure 9a) and integrated intensity in tensile direction (Figure 9b), which indicates the occurrence of cavitation during deformation of the 70/30 blend. However, from comparison of the absolute integrated intensity values with those of the 80/20 blend, it can be concluded that the amount of cavitation is very limited (compare Figures 7b and 4.9b). For PMMA/epoxy blends with an even higher rubber content, cavitation does not occur at all as can be concluded from both the scattering patterns (Figure 4d) and the azimuthal plot (Figure 10) of the 50/50 blend. Generally, both the 70/30 and the 50/50 blend deform via shear yielding without the necessity of preceding cavitation.

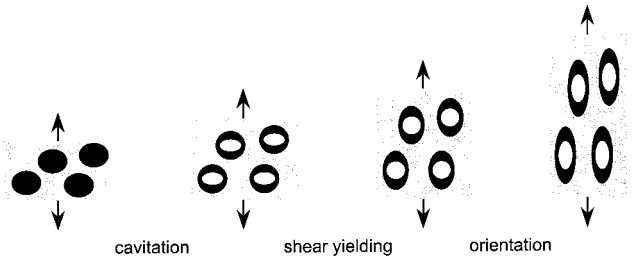

Figure 8. Schematic representation of the development of cavitation induced shear yielding in PMMA/epoxy 80/20 as derived from the in-situ SAXS deformation experiments.

It is evident that the scattering patterns observed for these blends should be attributed to the orientation of the rubber morphology. Comparison of the absolute integrated intensities of the PMMA/epoxy 90/10 and 70/30 blends confirms that the scattering is indeed caused by the electron density difference between the PMMA and epoxy phase. The initial integrated intensity values of the 70/30 blend is roughly 10 times higher than the 90/10 blend which is considered to be homogeneous and thus does not possess any separate rubber phase at all. Consequently, the limited scattering observed for the blends possessing more than 10 wt % epoxy has to be the result of the electron density difference between the rubber and PMMA phase. Therefore, the changes in the scattering patterns during drawing are the result of the orientation of the rubber and PMMA matrix.

The local strain plotted in Figure 9c is comparable to that of the 80/20 blend, Figure 7c. During the first stage of the clamp displacement hardly any plastic deformation is observed. Next, the local strain starts to increase at a strain rate which slowly levels off upon further drawing. Although the drawing process was terminated before fracture had occurred, the maximum strain observed again approached 150%, which is in agreement with the values obtained in the macroscopic tensile test.[5] In contrast to the 80/20 blend, no sudden changes at the end of the deformation process are observed as result of the premature ending of the test prior to fracture.

4.4. Influence of the Rubber Phase. For comparison, the deformation behavior of a PMMA/epoxy 80/20 blend, for which the epoxy is not cross-linked during polymerization, has been investigated. To avoid the cross-linking during polymerization instead of using a diamine as curing agent, a similar monofunctional amine (3-isopropoxypropylamine) is used in a stoichiometric amount. Though, this results in formation of uncross-linked epoxy, chemically induced phase separation still occurs during the simultaneous polymerization of the MMA and epoxy.

Figure 4e shows the development of the scattering patterns during tensile deformation of this blend. As is evident, the mode of microscopic deformation is completely different from the 80/20 blend with a cross-linked epoxy phase (compare Figures 4b and 4e). In Figure 4e, first a strong scattering streak is observed in the tensile direction, $x = 0.48$, followed by the development of a second streak perpendicular to the tensile direction, x

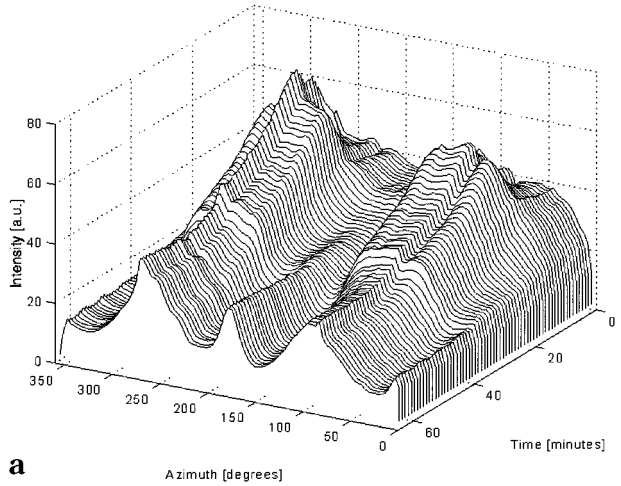

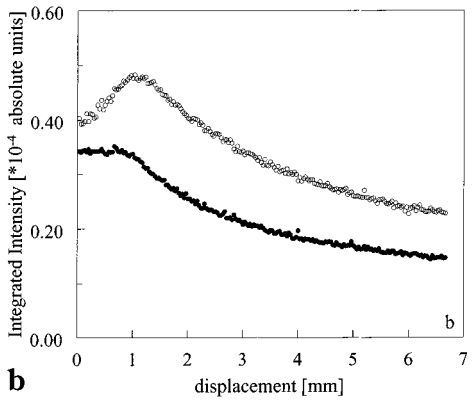

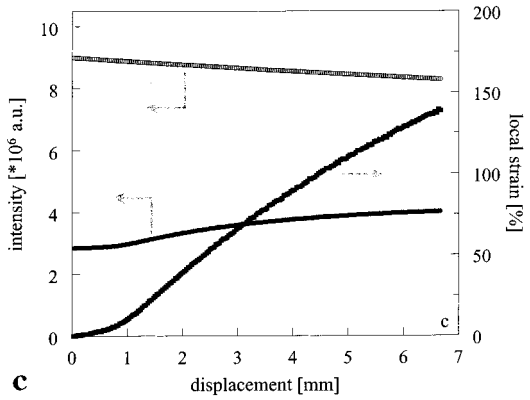

Figure 9. SAXS data for the in-situ deformation of PMMA/epoxy 70/30, stretching speed of the sample was 0.1 mm/min: (a) azimuthal plot (ESRF), (b) absolute intensity integrated perpendicular (●) and parallel (○) to the tensile direction vs the clamp displacement (CLRC), (c) local strain (■), intensity of the first (○) and second (●) ionization chamber vs clamp displacement (CLRC).

= 0.65. As discussed, the mode of microscopic deformation for these types of typical scattering patterns can be identified as crazing. Although this suggests a brittle macroscopic mechanical behavior, very stable crazes appear to be formed which allows for the development of an unique craze SAXS pattern, $x = 1.3$. However, the incoming of scattered intensity between the principal axis may suggest the occurrence of some cavitation during the later stage of the drawing process.

The remarkable feature observed in Figure 11 is the strong intensity of the craze fibril scattering which even approaches that of the streak in the tensile direction. The most probable explanation for this phenomenon is

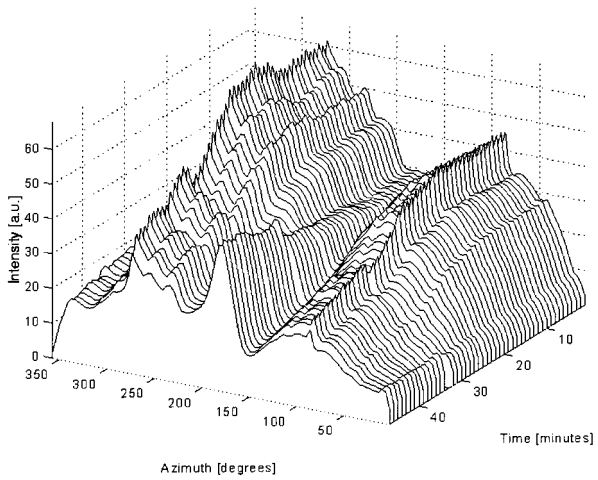

Figure 10. Azimuthal plot for the in-situ deformation of PMMA/epoxy 50/50 (ESRF). The deformation speed of the sample was 0.1 mm/min.

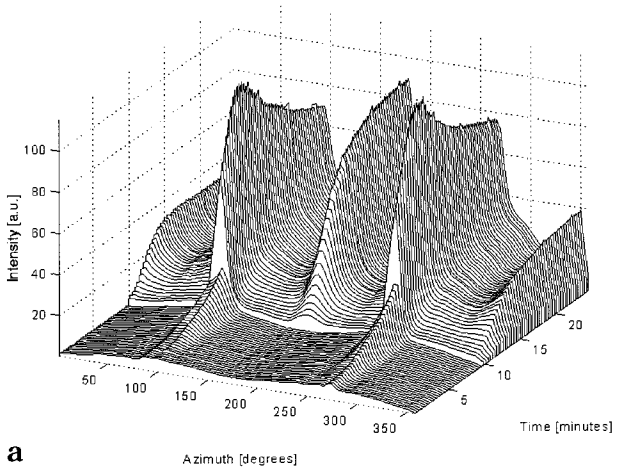

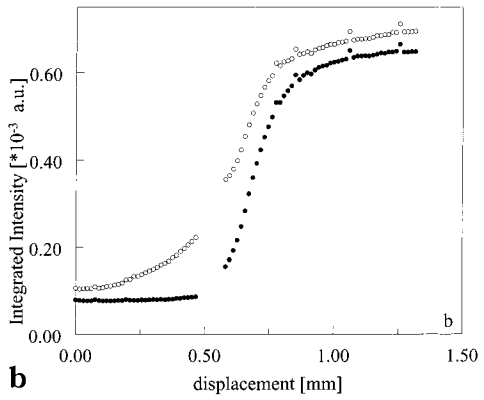

Figure 11. SAXS data for the in-situ deformation of PMMA/epoxy 80/20 for which the epoxy phase is not cross-linked (ESRF), the deformation speed of the sample was 0.05 mm/min: (a) azimuthal plot; (b) relative integrated intensity perpendicular (●) and parallel (○) to the tensile direction vs the clamp displacement.

the local plasticizing of crazes during deformation.[35,36] This results in the formation of many crazes with a large concentration of extremely stable craze fibrils. As a craze tip proceeds, it intersects with the low molecular weight epoxy droplets that plasticize the borders of the craze and, subsequently, enhance its development and stability. In the following section the craze fibril diameter for several samples and the influence of plasticizer on the fibril diameter is determined, with

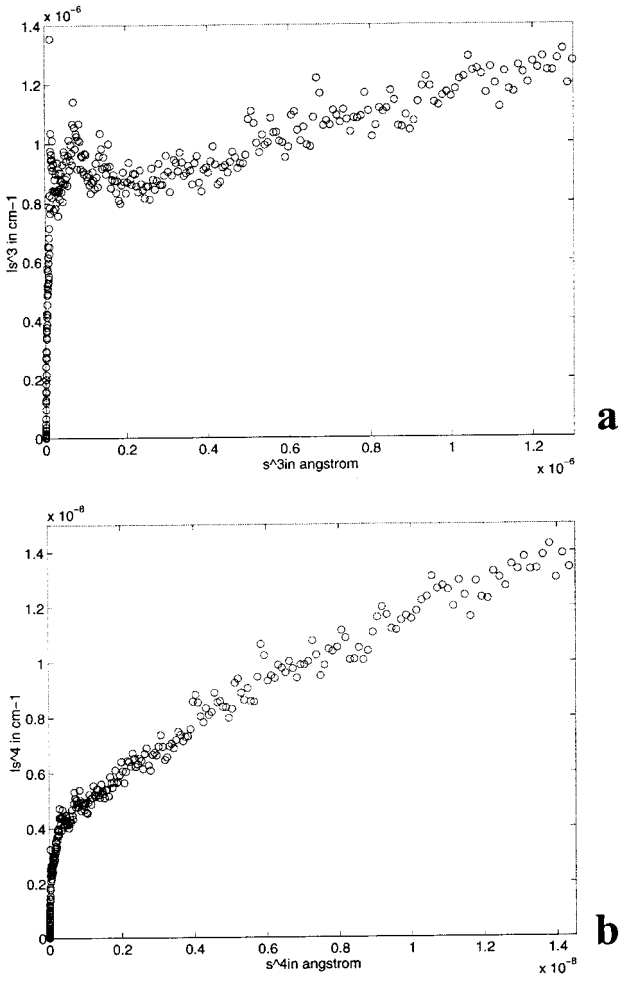

Figure 12. Figures here are plotted to determine Porods constant for the blend PMMA/epoxy 80/20 epoxy phase not cross-linked. The intensity along the *y*-axis in both figures is in absolute scale. The Porod constant in Figure 12a, $k = 8.1 \times 10^{-7}$ cm^{-1} is determined by plotting $s^3I(s)$ vs s^3, whereas the constant $k = 5.0 \times 10^{-9}$ cm^{-1} is determined by plotting $s^4I(s)$ vs s^4, as shown in Figure 12b.

the help of mathematics laid in section 3.1.2 of this paper.

4.5. Determination of the Craze Fibril Diameter within Crazes. With the help of eq 2, $D = 1/[\pi^3(1 - \nu)](Q_{eq}/k)$, in section 3.1.2 the craze fibril diameter was determined. Just to recapitulate in eq 2, D is the fibril diameter and n the volume fraction of the fibrils within the crazes. With the help of electron micrographs n is estimated to be 0.5, in general (for reference see Kramer et al.). This value has been used for our purposes also. The invariant, Q_{eq}, is determined for the scattered intensity arising from the craze fibrils, especially when the sample is fully stretched. Since at the low angles the invariant will be least influenced, the conventional method of extrapolating the intensity to zero angles by simply drawing a straight line from the minimum recorded scattering angle ($s_{min} = 0.0024$ nm^{-1}) to zero angle is used, whereas the maximum recorded scattering angle s_{max} was 0.0988 nm^{-1}. The values quoted for the scattering angles are for the detector radius 90 mm, sample−detector distance 8 m, and X-ray wavelength 0.1 nm used at ID2-BL4 (ESRF, Grenoble). The data for the present studies were obtained using this beamline. The Porod constant k is determined by plotting $s^3I(s)$ vs s^3 (see Figure 12a) (or $s^4I(s)$ vs s^4 , see Figure 12b; a reason for this variation in approach is given in the note or ref 31).

Table 2. Craze Fibril Diameter of the Crazing Systems, Calculated via the Porod Analysis

material	craze fibril diam [nm]	std dev [nm]
PMMA/epoxy 90/10	6.6	0.6
extrusion PMMA VO52	6.8	0.7
cast PMMA	7.6	1.1
PMMA/epoxy 80/20 epoxy phase is *not* cross-linked	5.1	0.08

The Porod constant as determined from Figure 12a is of the magnitude 8.1×10^{-7} cm^{-1}, whereas the one determined from Figure 12b is 5.0×10^{-9} cm^{-1}; the invariants determined for the two different approaches are 6.471×10^{-4} cm^{-1} (from section 3.1.2, eq 1d) and 3.98×10^{-6} cm^{-1} (from the equation for the invariant in ref 31), respectively.

It is to be noted that

$$\text{for } s^3I(s) \text{ vs } s^3, \quad k/Q_{eq} = 1.23 \times 10^{-3}$$

$$\text{for } s^4I(s) \text{ vs } s^4, \quad k/Q_{eq} = 1.25 \times 10^{-3}$$

Thus, the value for the diameter of the craze fibril as calculated quantitatively here is hardly influenced by this variation. Similar, minor variations are observed by adopting the two different approaches for determining the Porod constant and the invariant for the other samples, whose craze fibril diameters are calculated and summarized in Table 2.

According to the few studies reported concerning craze plasticizing, the craze fibril diameter is expected to increase in comparison to unplasticized systems. However, the fibril diameter of the crazing systems discussed, PMMA and PMMA/epoxy 90/10, is approximately 7 nm and appears to decrease to 5 nm for the PMMA/epoxy 80/20 blend with un-cross-linked epoxy (see Table 2). The reason for this difference is rather unclear but clearly demonstrates the ability of low molecular weight rubbers or solvents to influence the craze morphology. Additionally, the experiments show that the epoxy phase should be cross-linked to a maximum extent in order to avoid crazing.

5. Conclusions

The macroscopic synergistic toughening effect observed for the PMMA/epoxy blends is accompanied by several different types of microscopic deformation mechanisms, depending on the rubber content. The homogeneous and brittle 90/10 blend deforms via the formation of crazes that appear to be much more stable in comparison to those in neat PMMA. Blends with a higher rubber content are macroscopically more ductile, and all deform via shear yielding. In the case of the 80/20 blend, shear yielding is promoted by the preceding cavitation process which relieves the triaxial stress state and explains the macroscopically observed stress whitening.[27,28] In contrast, at even higher rubber fractions, cavitation, and the resulting macroscopic stress whitening, does not occur, and shear yielding is the most important deformation process. The scattering patterns observed are mainly the result of the orientation of rubber particles and PMMA matrix and thus the electron density differences between the rubber and PMMA phase.

The importance of a cross-linked epoxy phase is clearly demonstrated by the 80/20 blend for which the epoxy phase has not been cross-linked during polymerization. The mode of microscopic deformation changes from cavitation-induced shear yielding to crazing. The unusual strong fibril scattering observed (compare Figures 4e and 11) indicates the development of extremely stable craze fibrils which are most probably the result of the local plasticizing of craze by the un-cross-linked low molecular weight epoxy rubber.

The proposed calculation of the local strain is successfully used to explain the relation between the scattering patterns and the extent of deformation in the beam spot. The calculated strains are in accordance with the results of the macroscopic mechanical tensile tests. For the 90/10 blend it is revealed that crazing is not initiated for a strain less than 2.5% and that the local strain rate decreases after the initiation and growth of the crazes. The sensitivity of the calculation procedure is demonstrated by the experiment involving the 80/20 blend where sample thickening was detected prior to fracture as a result of macroscopic crack initiation outside the beam spot.

Generally, the simultaneous SAXS deformation experiments are a powerful method to study the different deformation mechanisms and their development upon drawing. Since the 80/20 blend deforms via cavitation, it offers the possibility to study the influence of submicron voids on the mechanical behavior of brittle amorphous polymers that were the subject of papers published recently.[21,22]

Acknowledgment. The authors are grateful for availability of the beamline ID2/BL4 at the European Synchrotron Radiation Facility (ESRF, Grenoble, France). Especially the experimental support of Dr. P. Boesecke is acknowledged together with the assistance of Dr. A. Hammersley in the analysis of the data with the help of the FIT2D software program, developed at the ESRF. The authors thank Prof. A. J. Ryan, Dr. P. Fairclough (University of Sheffield, UK), Dr. Nick Terrill, and Mr. A. Gleeson (SRS, CLRC, Warrington, UK) for their experimental contributions on station 2.1 at the Synchrotron Radiation Source (SRS, Warrington, UK). Furthermore, the authors thank Professor Edward J. Kramer (University of California at Santa Barbara) for his very constructive comments which have helped shape the manuscript to its current form.

References and Notes

(1) Bucknall, C. B. *Toughened Plastics*; Applied Science Publishers Ltd.: London, 1977.
(2) Sanden van der, M. C. M.; Meijer, H. E. H.; Lemstra, P. J. *Polymer* **1993**, *34*, 2148.
(3) Smit, R. J. M.; Meijer, H. E. H.; Brekelmans, W. A. M.; Govaert, L. E. *J. Mater. Sci.*, submitted.
(4) Smit, R. J. M. Ph.D. Thesis, Eindhoven University of Technology, 1998.
(5) Jansen, B. J. P.; Meijer, H. E. H.; Lemstra, P. J. *Polymer*, part 1 of this series, submitted.
(6) Bubeck, R. A.; Buckley, D. J.; Kramer; Brown, H. R. *J. Mater. Sci.* **1991**, *26*, 6249.
(7) Buckley, D. J., Jr. Ph.D. Thesis, Cornell University, 1993.
(8) He, C.; Donald, A. M.; Butler, M. F.; Diat, O. *Polymer* **1998**, *39*, 659.
(9) He, C.; Donald, A. M.; Butler, M. F. *Macromolecules* **1998**, *31*, 158.
(10) Lovell, P. A.; Ryan, A. J.; Sherratt, M. N.; Young, R. J. *Polym. Mater. Sci. Eng.* **1994**, *70*, 155.
(11) Ijichi, Y.; Kojima, T.; Suzuki, Y.; Nishio, T.; Kakugo, M. *Macromolecules* **1993**, *26*, 829.
(12) Okamoto, Y.; Miyagi, H.; Uno, T.; Amemiya, Y. *Polym. Eng. Sci.* **1993**, *33*, 1608.
(13) Butler, M. F.; Donald, A. M.; Ryan, A. J. *Polymer* **1997**, *38*, 5521.
(14) Butler, M. F.; Donald, A. M.; Ryan, A. J. *Polymer* **1997**, *39*, 781.
(15) Butler, M. F.; Donald, A. M.; Bras, W.; Mant, G. R.; Derbyshire, G. E.; Ryan, A. J. *Macromolecules* **1995**, *28*, 6383.
(16) Hughes, D. J.; Mahendrasinngam, A.; Oatway, W. B.; Heeley, E. L.; Martin, C.; Fuller, W. *Polymer* **1997**, *38*, 6427.
(17) Paredes, E.; Fischer, E. W. *Macromol. Chem.* **1979**, *180*, 2707.
(18) Brown, H. R.; Kramer, E. J. *J. Macromol. Sci., Phys.* 1981, *B19*, 487.
(19) Magalhaes, A. M. L.; Borggreve, R. J. M. *Macromolecules* **1995**, *28*, 5841.
(20) Jansen, B. J. P.; Meijer, H. E. H.; Lemstra, P. J. *Polymer* **1999**, *40*, 2917.
(21) Jansen, B. J. P.; Rastogi, S.; Meijer, H. E. H.; Lemstra, P. J. *Macromolecules* **1999**, *32*, 6283.
(22) Jansen, B. J. P.; Rastogi, S.; Meijer, H. E. H.; Lemstra, P. J. *Macromolecules* **1999**, *32*, 6290.
(23) Russel, T. P.; Lin, J. S.; Spooner, S.; Wignall, G. D. *J. Appl. Crystallogr.* **1988**, *21*, 629.
(24) http://srs.dl.ac.uk/ncd/station21 and http://www.esrf.fr/exp_facilities/ID2/handbook/handbook.html.
(25) Kratky, O.; Pilz, I.; Schmitz, P. J. *J. Colloid Interface Sci.* **1966**, *21*, 24.
(26) Stribeck, N. ACS Symposium Series, PMSE Meeting, Boston, Aug 1998.
(27) Stribeck, N. *Macromolecules* **1996**, *29*, 7217.
(28) It is to be noted that though the separation of the invariants into a meridional and an equatorial component is a useful approximation insofar as the scattering functions for the two different mechanisms are concentrated in the different sectors. It need to be mentioned that in doing so an approximation has been taken into account that the particulate scattering from any one mechanism generally contributes some intensity throughout all of the reciprocal space.
(29) Brown, H. R. *Mater. Sci. Rep.* **1987**, *2*, 315.
(30) Glatter, O.; Kratky, O. *Small-Angle X-ray Scattering*; Academic Press: London, 1982; Chapters 2 and 4.
(31) However, the contention that the proper function for assessing intensity variation should be s^{-3}, opposed to s^{-4}, often leads to several objections, because the literature on the Porod invariant for anisotropic scatterers is still in its infancy, so that the question of calculating it remains open. In this paper we have no inclination to resolve this basic issue. We have adopted the approach, generally accepted in the literature for the craze fibrils by the previous workers whose work has been accepted by the community with the arguments stated in the above paragraph. But to give justice to the other possibilities we have shown the plots for $s^3I(s)$ vs s^3 and $s^4I(s)$-vs s^4 and has determined the Porods' constant K from the both curves. But to determine the craze fibril diameter, from eq 1e, for Porods' constant determined by plotting the curve $s^4I(s)$ vs s^4, the formulas used for the invariant need to be modified. The general nature of the formulas would then be $Q_{eq} = 2\int_0^\infty I(s_{12})\, ds_{12}$, where $I(s_{12}) = \pi s^2 12 \int_{s_3=-s_{12}}^{s_3=s_{12}} I(s_{12},s_3)\, ds_3$. A comparison of the diameter of the fibrils determined by two different routes is given in section 4.5. It is to be noted that hardly any difference is observed for determining the craze fibril diameter, as calculated by adopting the two different routes.
(32) Pearson, R. A.; Yee, A. F. *J. Mater. Sci.* **1991**, *26*, 3828.
(33) Bagheri, R.; Pearson, R. A. *Polymer* **1996**, *37*, 4529.
(34) Gebizlioglu, O. S.; Beckham, H. W.; Argon, A. S.; Cohen, R. E.; Brown, H. R. *Macromolecules* **1990**, *23*, 3968.
(35) Argon, A. S.; Cohen, R. E.; Gebizlioglu, O. S.; Brown, H. R.; Kramer, E. J. *Macromolecules* **1990**, *23*, 3975.

MA001810Y